Ore Geology Reviews 160 (2023) 105584

Contents lists available at ScienceDirect

Ore Geology Reviews

journal homepage: www.elsevier.com/locate/oregeorev

Mica geochemistry as an indicator of magmatic-hydrothermal processes in the Ta-Nb-Sn-W mineralization of the Limu deposit, South China

Hong-Wei Peng [a,b], Ling-Li Yang [b], Jian-Qing Lai [b,*], Bin Li [b], Xiang-Hua Liu [b,c], Zhi-Hui Dai [a]

[a] State Key Laboratory of Ore Deposit Geochemistry, Institute of Geochemistry, Chinese Academy of Sciences, Guiyang 550081, China
[b] Key Laboratory of Metallogenic Prediction of Nonferrous Metals and Geological Environment Monitoring (Ministry of Education), School of Geosciences and Info-physics, Central South University, Changsha 410012, China
[c] School of Civil Engineering and Architecture, Guangxi Minzu University, Nanning 530007, China

ARTICLE INFO

Keywords:
Mica geochemistry
Magmatic process
Hydrothermal process
Ta-Nb-Sn-W mineralization
Limu deposit

ABSTRACT

Limu deposit is one of the representative deposits with coexisting Ta-Nb and Sn-W mineralization in the Nanling Range, South China. It consists of three stages of granites, with the Ta-Nb and Sn-W mineralization mainly restricting in the third-stage granite. However, the details of the polymetallic mineralization process in this deposit are still obscure. This study utilizes mica geochemistry to trace the ore-related magmatic and hydrothermal processes. The primary micas evolved from Li-phengite in the first- and second-stage granites to zinnwaldite-lepidolite in the third-stage granite. The micas are increasingly enriched in Li, F, Rb and Cs elements with decreasing K/Rb and K/Cs ratios, suggesting a dominant fractional crystallization of feldspars, particularly plagioclase, with minor mica fractionation during magma evolution. The Li-phengites from the first- to the second-stage granites increase in Ta (average value: 38 to 61 ppm) and Nb concentrations (average value: 160 to 180 ppm) but decrease in Nb/Ta ratios (average value: 4.4 to 3.5), consistent with the bulk-rock Ta-Nb enrichment trends. However, the zinnwaldite in the third-stage granite has significantly lower Nb (110 ppm in average) but higher Ta concentration (170 ppm in average), and evolves to lepidolite toward decreasing Nb and Ta concentration (51 and 63 ppm in average, respectively) and increasing Nb/Ta ratios (average value: 0.7 to 1.0). These chemical features of the micas are controlled by co-crystallization of columbite group minerals (CGM) during the evolution of third-stage granitic magma, which was likely Nb-rich at the early stage and evolved toward Ta enrichment. Thus, magmatic processes played a critical role in the Ta-Nb mineralization. Secondary hydrothermal micas in the third-stage granite distinctly depleted in Li, F, Rb and Cs recrystallized from the primary zinnwaldite-lepidolite via replacing reaction, which are closely associated with cassiterite, wolframite and pyrite in the granite. The consistent $\delta^{34}S$ values of the disseminated pyrite (0.71‰) and vein-type pyrite (1.12‰) in the granite indicate that the hydrothermal system was dominated by magmatic fluids without notable involvement of external fluids. The lower Ta and Nb concentrations (31 and 35 ppm in average, respectively) of the hydrothermal micas compared to primary ones suggest that at least small amounts of Ta and Nb were transferred by the fluids. Indicated by the mica concentrations, Sn and W were enriched with magma evolution and likely concentrated in the volatile and flux components of the third-stage magma. Furthermore, cassiterite and wolframite in the granite precipitated by fluid-rock interaction, and a portion of W and Sn migrated away with exsolved fluids to form the quartz vein W-Sn mineralization. This study demonstrates that mica geochemistry can effectively indicate magmatic-hydrothermal processes in granite-related Ta-Nb and Sn-W mineralization.

1. Introduction

Tantalum (Ta) and niobium (Nb) are critical strategic metals due to their wide use in electronic devices and high-performance alloys (Linnen et al., 2012). Although the majority of Ta is mined from LCT-type pegmatites, rare metal granites are an important source for Ta and Nb (Linnen et al., 2012), which are commonly enriched in flux components such as Li, F and P (e.g., Li et al., 2015; Michaud et al., 2020; Pollard,

* Corresponding author.
E-mail address: ljq@csu.edu.cn (J.-Q. Lai).

https://doi.org/10.1016/j.oregeorev.2023.105584
Received 20 February 2023; Received in revised form 11 July 2023; Accepted 22 July 2023
Available online 24 July 2023

2021), and are usually developed with W and Sn mineralization. The Ta, Nb, W and Sn (divalent) all behave as incompatible elements in magmatic processes, and can therefore be enriched in residual melts by high degrees of magma differentiation. For Ta-Nb mineralization, a critical role of magmatic processes has been acknowledged (Linnen and Cuney, 2005; Van Lichtervelde et al., 2007; Linnen et al., 2012; Kaeter et al., 2018; Wu et al., 2018; Michaud et al., 2020; Pollard, 2021). However, it is still debatable whether magmatic processes are sufficient in generating the mineralization, or whether hydrothermal processes also play a role and their importance relative to magmatic processes (Van Lichtervelde et al., 2007). In addition, Ta-Nb fractionation is commonly observed to occur in Ta-Nb mineralized granites (e.g., Černý et al., 1985, 1986; Anderson et al., 2013; Melcher et al. 2017; Wu et al., 2018), but the controls regarding the fractionation are still an area of active research. By contrast, W-Sn mineralization is more closely correlated with hydrothermal processes, which can occur within granite roof, and in metasomatic zones of granite (greisen), and as quartz veins in periphery country rocks (Černý et al., 2005). Such diversity of W-Sn mineralization makes its relationship with Ta-Nb mineralization ambiguous.

Micas are useful petrogenetic indicator of magma evolution, in that they generally crystallize throughout entire magmatic processes with significant composition evolution (e.g., Tischendorf, 1997; Van Lichtervelde et al., 2008; Li et al., 2015, 2021). Micas from rare metal granites are commonly characterized by enrichments of flux components of Li and F, and Rb and Cs, the concentrations and ratios (e.g., K/Rb and K/Cs) of which are chemical markers of magma differentiation (London, 2022). In addition, mica is compatible with Ta and Nb and can also incorporate considerable W and Sn, and therefore its Ta-Nb and W-Sn concentration variations can reflect concentrating processes of these elements in magmatic processes. Moreover, fractional crystallization of micas was claimed to play a critical role in Ta-Nb fractionation in magma systems (Stepanov et al., 2014). Noticeably, secondary metasomatic mica usually occurs in rare metal granites in response to post-magmatic hydrothermal processes. Numerous studies have shown that chemical features of the hydrothermal micas can effectively indicate fluid sources and evolutions with respect to W-Sn mineralization, and can also evaluate the potential role of hydrothermal processes in Ta-Nb mineralization (Van Lichtervelde et al., 2008; Li et al., 2015, 2021; Legros et al., 2018; Yin et al., 2019; Wei et al., 2020). To sum up, mica geochemistry is expected to serve as an excellent indicator of magmatic-hydrothermal processes in granites and related Ta-Nb and W-Sn mineralization.

The Limu deposit is located in the western Nanling Range, western Cathaysia block. Different from most deposits in the Nanling Range hosting W or Sn mineralization without significant Ta-Nb mineralization, it is one of the representative deposits with coexisting considerable Ta-Nb and W-Sn mineralization, with a total estimated reserves of ca. 4670 t Ta_2O_5, 4440 t Nb_2O_5, 50000 t Sn and 18900 t WO_3. The deposit is predominantly composed of a granite complex with three petrogenetic stages, that are consecutive in age and genetically linked (Zhu et al., 2001; Feng et al., 2019; Huang et al., 2020). Noticeably, the third-stage granite is the most ore-producing, where the disseminated Ta-Nb and Sn-W mineralization occurs in the uppermost part of the granite and the quartz vein type W-Sn mineralization occurs in sedimentary country rocks. Thus, the Limu deposit is an excellent natural laboratory for probing into the relative importance of magmatic and hydrothermal processes in generating the Ta-Nb and Sn-W mineralization in rare metal granites and the genetic relationship between two types of mineralization. However, previous studies mainly focused on petrology and geochronology of the granites and mineralization, with little study about the ore-forming processes and controls on the Ta-Nb and Sn-W mineralization. Ma et al. (2020) identified magmatic and hydrothermal micas in one stock of the third-stage granite, and pointed out a critical role of external fluids in Sn mineralization hosted in the granite based on chemical evolution of the micas. However, their study leaves the micas from the first- and second-stage granites and the information of Ta-Nb enrichment and mineralization in the third-stage granite open for further investigation. Besides, secondary hydrothermal micas were identified in granites of the Limu deposit as well as other deposits in the Nanling Range, whereas, it seems to remain controversial on the source of the hydrothermal fluids accounting for the secondary micas, particularly on magmatic vs. external fluids.

In this study, we focus on micas from the three stages of granites at the Limu deposit, and combine petrography and electron probe microanalyzer (EPMA) and laser ablation-inductively coupled plasma-mass spectrometry (LA-ICP-MS) analyses of micas with bulk major and trace element analyses of granites to reveal magma evolution, and magmatic and hydrothermal processes related to Ta-Nb and Sn-W mineralization, with LA-multicollector (MC)-ICP-MS sulfur isotope analyses of pyrite in granites to constrain fluid source.

2. Regional and deposit geology

The Limu Ta-Nb-Sn-W deposit is located in the western Nanling Range, South China block (Fig. 1). The South China block comprises the Cathaysia block in the southeast and the Yangtze block in the northwest, which amalgamated along the Jiangnan Belt during Neoproterozoic (e.g., Zhao and Cawood, 2012). The South China block contains Precambrian basement rocks that are mainly Paleoproterozoic and Neoproterozoic in age (Zhao and Cawood, 2012), and is characterized by several periods of large-scale tectono-magmatism from Paleozoic to Mesozoic (e.g., Zhou et al., 2006; Li and Li, 2007; Wang et al., 2013). During Mesozoic, the Indosinian (Triassic) and Yanshanian (Jurassic-Cretaceous) magmatism were mainly developed in the Cathaysia block (Fig. 1; Zhou et al., 2006). The Indosinian granites is predominantly distributed in the inland region of the Cathaysia block and the border region with the Yangtze block, whereas the massive Yanshanian granites and volcanic rocks are distributed in the Cathaysia block towards the coast (Fig. 1). Although it remains highly debated on the petrogenesis and tectonic domain of the large-scale Indosinian and Yanshanian magmatism, a commonly accepted viewpoint is that the two periods of magmatism were formed under extension settings (e.g., Zhou et al., 2006; Li and Li, 2007; Wang et al., 2013).

The Nanling Range is located in the central-western part of the Cathaysia block (Fig. 1). It is characterized by massive Yanshanian granitic magmatism in the central-eastern part and Indosinian granites in northern part, with some relatively small-scale Indosinian granites in western part, such as Dupangling and Limu. The Nanling Range is a world-renowned W-Sn metallogenic province, and also an important source region for rare metals such as Nb-Ta, Li, Be and Rb (e.g., Mao et al., 2013; Wang et al., 2020). The vast majority of W-Sn and rare-metal mineralization in the Nanling Range is genetically related to the Yanshanian granites, and a minor part is related to the Indosinian granites (e.g., Mao et al., 2013; Chen et al., 2014; Yuan et al., 2019; Wang et al., 2020), with Limu being one of the largest and representative Indosinian granite-related Ta-Nb-Sn-W deposit.

In the Limu mining district, Cambrian basement rocks mainly comprising low-grade metamorphic marine flysch sequences are developed in the west region, and a series of Devonian-Carboniferous sedimentary covers composed of sandstone-shale and carbonate rocks crop out with large areas in the central and eastern regions (Fig. 2a). Three groups of faults occur in the district, including N-S-trending, E-W-trending and SW-NE-trending faults, where the N-S-trending ones prevail and appear to be the controlling structures for emplacement of granitic magmatism and related mineralization (Fig. 2a). An Indosinian granite complex intrudes into the Devonian-Carboniferous sequences and Cambrian basement rocks (Fig. 2), which occurs as stocks cropping out with ca. 1.5 km^2 and emplacing underground with ca. 8 km^2 revealed by drilling holes (Zhu et al., 2001). The granite complex is acknowledged to be composed of three stages, and is developed with Ta-Nb-Sn-W polymetallic mineralization (Zhu et al., 2001; Feng et al.,

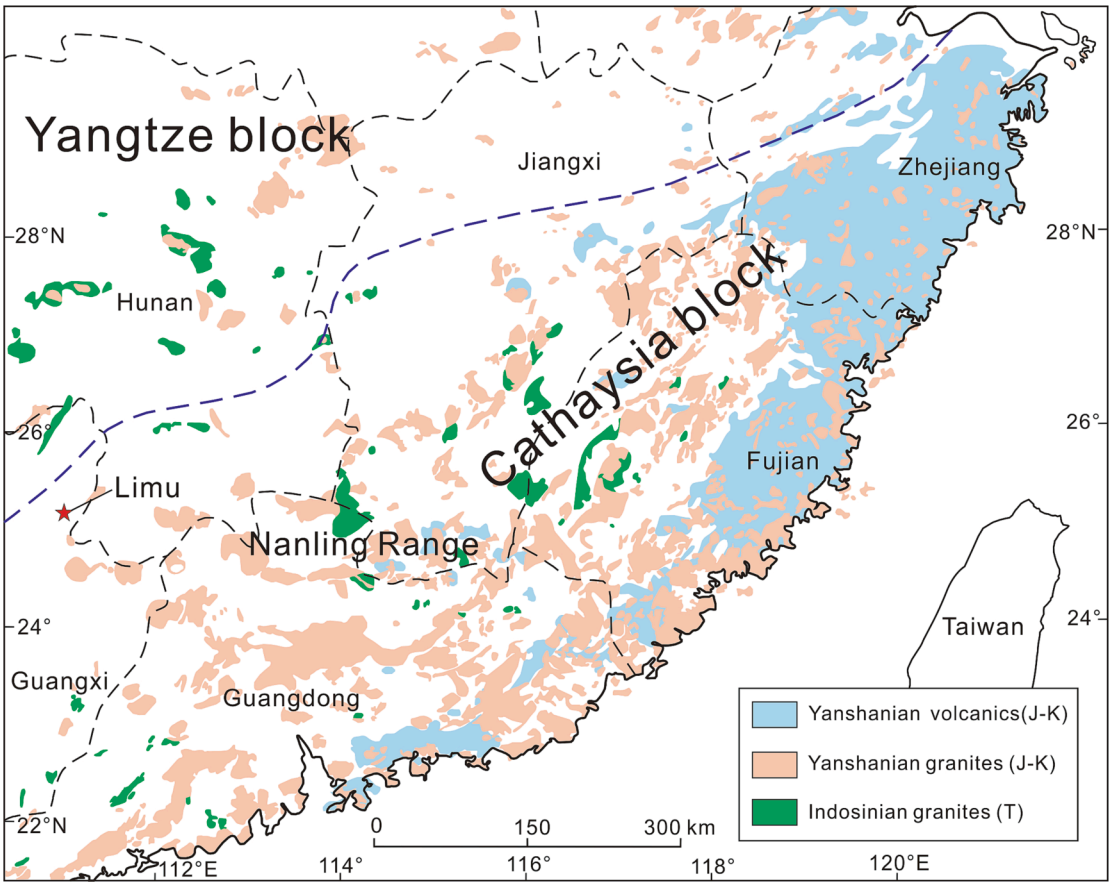

Fig. 1. Simplified geological map of the Cathaysia block showing the distribution of Indosinian granites and Yanshanian granites and volcanic rocks and the location of the Limu deposit (modified after Zhou et al., 2006).

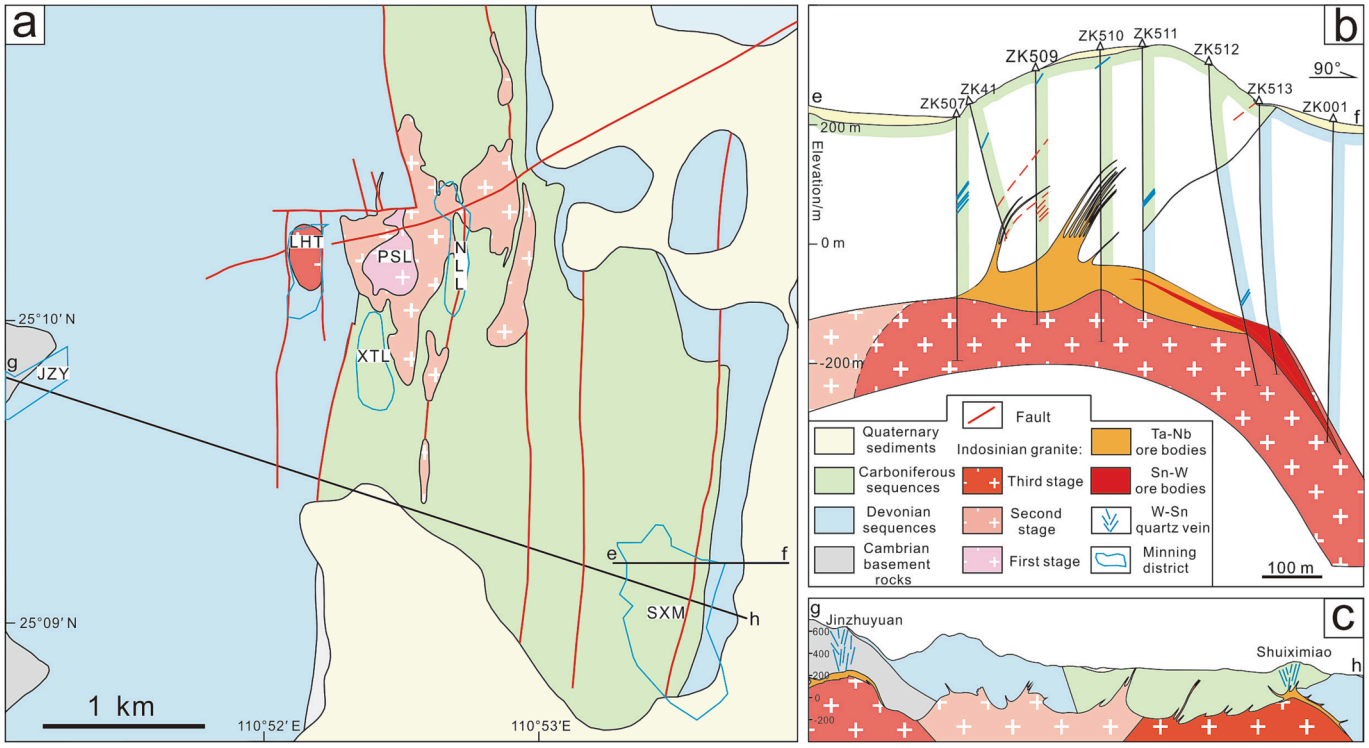

Fig. 2. (a) Geological map of the Limu mining district; (b) The geological cross section of the Shuiximiao deposit from e to f in the Fig. 2a; (c) The geological cross section from g to h in the Fig. 2a. JZY = Jinzhuyuan, LHT = Laohutou, NNL = Niulanling, PSL = Paoshuiling, SXM = Shuiximiao, XTL = Xiangtanling.

2013, 2019; Huang et al., 2020).

The first-stage granite is distributed in Paoshuiling as a small stock with exposed area of ca. 0.1 km^2 (Fig. 2a), which is poor in metallic mineralization with variable kaolinization (Fig. 3a). The second-stage granite crops out with larger areas that encloses the first-stage Paoshuiling stock (Fig. 2a, c). The second-stage one is developed with quartz vein-type W-Sn deposits mainly at Niulanling, Xiangtanling (Fig. 2a), where ore-bearing quartz veins extend from the granites and intrude into overlying sedimentary country rocks. The third-stage granite is represented by an exposed stock at Laohutou and two unexposed stocks at Shuiximiao and Jinzhuyuan, which intrude into the second-stage granites (Fig. 2). The third-stage granite is the most ore-producing one, mainly including the Ta-Nb-Sn-W mineralization restricted in the granite roof occurring as disseminated ore minerals of CGM, cassiterite and wolframite, and the W-Sn mineralization as wolframite-cassiterite quartz (-feldspar) veins intruding into the overlying sedimentary country rocks (Fig. 2b, c). Typically, a vertical zonation with respect to geological features is developed with the third-stage granite, especially at Shuiximiao. From deep to shallow, the zonation is composed of albite granite and Ta-Nb-Sn-W topaz-albite granite to pegmatite-aplite dykes, W-Sn (feldspar-) quartz veins and fluorite-lepidolite veinlets hosted in the sedimentary country rocks (Fig. 2b, c; Zhu et al. 2001).

Previous studies have mainly focused on the geochronology of the Limu deposit and the petrology of the granites. The crystallization ages of the three stages of granites have been estimated by zircon U-Pb isotopic ages, that are ca. 231 ± 1 to 228 ± 5 Ma for the first stage, 225 ± 2 to 223 ± 1 Ma for the second stage, and 218 ± 2 to 212 ± 2 Ma for the third stage (Feng et al. 2013, 2019; Huang et al. 2020). The three stages of granites were revealed to have the same magma source of the Proterozoic basement rocks based on consistent Nd-Hf isotopic features (Huang et al., 2020). The Ta-Nb mineralized age of the Limu deposit is about 219 ± 3 to 217 ± 2 Ma estimated by U-Pb isotopic ages of CGM from the third-stage Shuiximiao and Jinzhuyuan stocks (Che et al., 2019), and the ages of hydrothermal Sn-W mineralization were estimated to be 214 ± 2 to 203 ± 3 Ma by hydrothermal muscovite Ar-Ar and hydrothermal zircons U-Pb ages (Feng et al., 2019; Huang et al., 2020).

3. Petrology

Samples of the first-stage granite were collected from outcrops of Paoshuiling granite, and the samples of the second stage were collected from drill holes, and the samples of the third-stage granite were collected from underground tunnels of the Shuiximiao deposit.

The first-stage Paoshuiling granite is light grey to white in color, and possesses fine-grained texture and massive structure with variable kaolinization (Fig. 3a). It consists of quartz (30 ~ 35 vol%), K-feldspar (30 ~ 35 vol%), plagioclase (25 ~ 30 vol%), mica (phengite to Li-phengite in composition from this study, ca. 5 ~ 8 vol%) and minor accessory minerals such as topaz, zircon and apatite (Fig. 3b). The K-feldspar and plagioclase are euhedral in shape with "dirty" appearance under microscope, and the plagioclase is mainly andesine to oligoclase in composition. The (Li-) phengite occurs as euhedral to subhedral flake crystals with relatively small size (mainly 100 ~ 600 μm in length), and show planar boundaries with the euhedral K-feldspar and plagioclase and anhedral quartz (Fig. 3b, c). It is generally colorless under plane-polarized light, and unzoned under BSE image (Fig. 3c).

The second-stage granite samples are light grey to light pink in color, medium-grained with massive and porphyritic-like texture (Fig. 3d). They comprise quartz (30 ~ 35 vol%), K-feldspar (ca. 25 ~ 30 vol%), plagioclase (30 ~ 35 vol%), mica (Li-phengite in composition from this study, ca. 5 vol%) (Fig. 3e) and minor accessory minerals of topaz, zircon and apatite. The CGM, wolframite and cassiterite occur occasionally in the granite, in which CGM occurs as euhedral crystals intergrown with the micas and feldspar, and wolframite and cassiterite replace the micas. The K-feldspar and plagioclase are euhedral in shape, in which the former locally occurs as phenocryst with large size, and the latter is andesine to albite (mainly oligoclase) with relatively smaller size. The Li-phengite, as euhedral to anhedral flake crystals with length mainly ranging from 200 to 1500 μm, commonly displays straight boundaries with the euhedral K-feldspar and plagioclase and anhedral quartz (Fig. 3e). It is colorless to light pink in color under plane-polarized light, and also commonly homogeneous (no zonation) in texture under BSE image (Fig. 3f).

The third-stage granite samples are light grey to white in color and

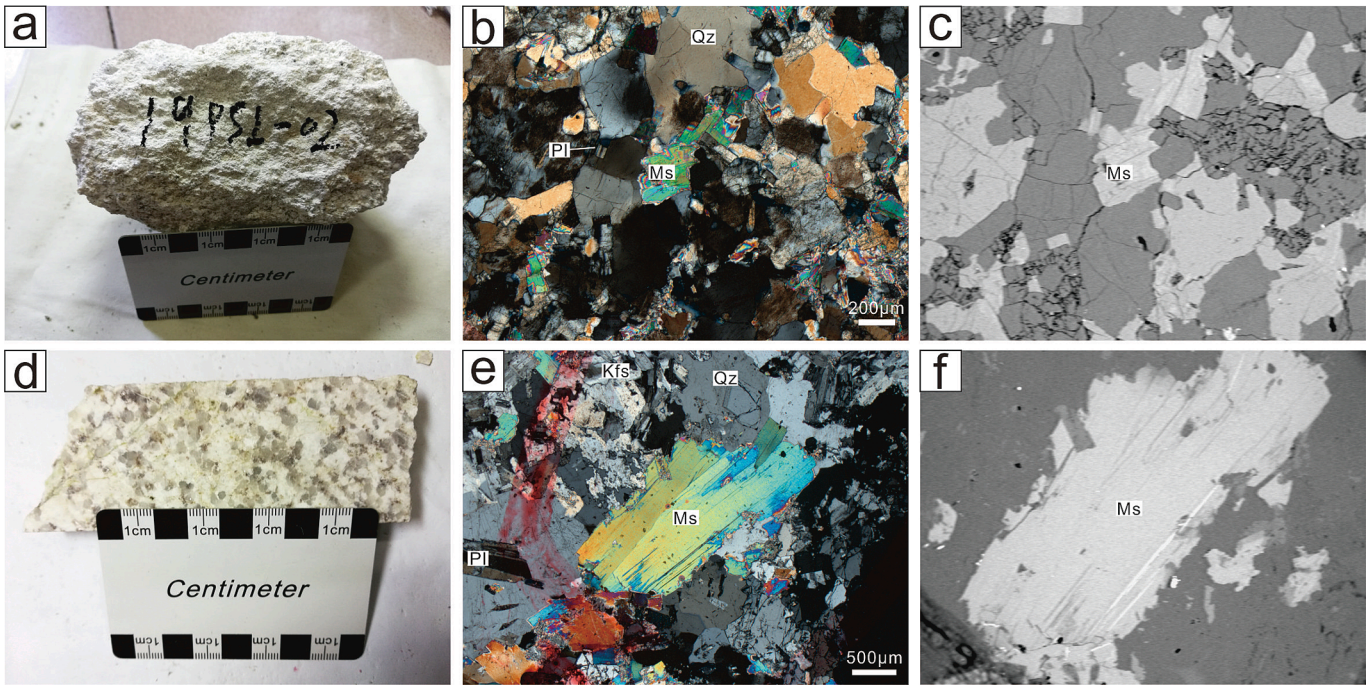

Fig. 3. Petrographic photographs of the first-stage granite (a-c) and the second-stage granite (d-f). (a, d) Hand specimen; (b, e) Rock-forming minerals assemblages; (c, f) SEM-BSE images of Fig. 3b and Fig. 3e showing uniform textures of the micas. Kfs = K-feldspar, Ms = muscovite, Qz = quartz.

exhibit fine-medium grained and massive texture (Fig. 4a). They are composed of quartz (25 ~ 35 vol%), K-feldspar (20 ~ 30 vol%), plagioclase (35 ~ 40 vol%), mica (mainly zinnwaldite to lepidolite with minor Li-phengite in composition from this study, ca. 5 vol%), topaz (variable 3 ~ 10 vol%) and minor accessory minerals such as CGM, apatite and zircon (Fig. 4), with some disseminated wolframite, cassiterite and pyrite (Fig. 4). The plagioclase is predominantly albite, and the K-feldspar is mainly microcline. The mica (zinnwaldite to lepidolite) is generally euhedral to anhedral crystals with flake shape that is mainly 200 to 1000 μm in length and colorless to light pink-brown-green in color under plane-polarized light (Fig. 4b-f). Texturally, it commonly shows planar boundaries with the euhedral K-feldspar and plagioclase and anhedral quartz (Fig. 4b-f). The zinnwaldite and lepidolite are almost indistinguishable by optical properties, but can be distinguished by texture under BSE image (Fig. 4d, e). They both occur as individual crystals, and sometimes, the relatively darker lepidolite overgrows the brighter zinnwaldite with planar boundaries formed (Fig. 4e, f). Noticeably, a Li-phengite is developed after the zinnwaldite and lepidolite (Fig. 4f), which is the darkest one under BSE image. It replaces the zinnwaldite and lepidolite as mica rims, with irregular boundaries cutting the cleavage of the zinnwaldite and lepidolite in the cores, and is associated with pyrite, cassiterite and wolframite also replacing the earlier zinnwaldite and lepidolite (Fig. 4f). The CGM is the principal ore mineral hosting Ta and Nb in the granite, and occurs as euhedral to subhedral columnar and polygonal crystals intergrown with the albite, mica and topaz, and is sometimes encompassed by mica and albite (Fig. 4b). Cassiterite and wolframite disseminate in the granite, which replace the zinnwaldite and/or lepidolite and usually concentratedly occur at areas where feldspars are altered by sericite (Fig. 4c, f, g), and also overgrow the CGM. Pyrite, usually intergrown with cassiterite and wolframite, also occurs in the granite (Fig. 4f) and locally develops into veins (Fig. 4g), which also replaces micas (Fig. 4f).

4. Analytical methods

4.1. Whole-rock major and trace element analyses

Whole-rock major and trace element analyses were conducted at the ALS Chemex (Guangzhou) Co Ltd. For major element analyses, mixtures of 200 mesh whole-rock powders and $Li_2B_4O_7$ were fused into glass discs at temperature higher than 1025℃, which were then analyzed by the Philips PW2404 X-ray fluorescence spectroscopy (XRF). Basaltic to granitic rock standards (NCSDC73303, SARM-2, SARM-3, and SARM-4) were analyzed to monitor the analytical error, which were within 2% in this study. For trace element analyses, the whole-rock powders were dissolved in distilled solution of $HF + HNO_3 + HClO_4$, dried, and then dissolved with HCl. The solutions were finally analyzed using an Agilent 7700x inductively coupled plasma mass spectrometry (ICP-MS). The analytical uncertainties are within 5% for most elements indicated by the analyses of standard materials of GBM908-10, MRGeo08, OREAS460 and SY-4, with detection limits for each element ranging from 0.01 to 0.1 ppm.

4.2. SEM and EPMA analyses

The internal textures of mica were observed with back-scattered electron (BSE) images using a TESCAN MIRA3 field-emission SEM at the Guangzhou Tuoyan Testing Technology Co. Ltd, Guangzhou, China.

The major and minor elements of mica were analyzed by a Shimadzu EPMA-1720H electron probe microanalysis (EPMA) at the School of Geosciences and Info-physics, Central South University , Changsha, China. An accelerating voltage of 15 kV, beam current of 10nA, and an electron beam diameter of 1 μm were used during analyses. The standards used for calibration included fluorite (F), albite (Na), biotite (Al, Ti, Fe, Mg, K), diopside (Si, Ca), rhodonite (Mn), pollucite (Rb). The resulting data were then ZAF corrected and the reproducibility of standard analyses was 1% to 5% for each element analyzed.

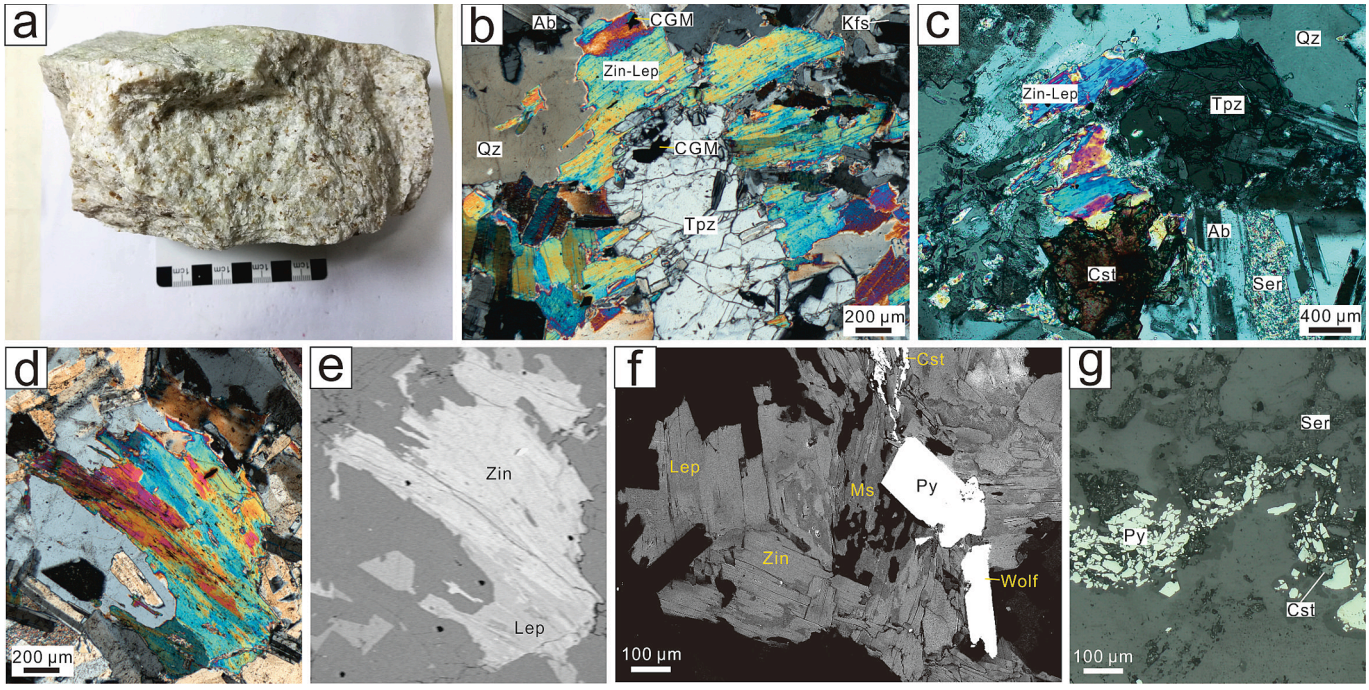

Fig. 4. Petrographic photographs of the third-stage granite. (a) Hand specimen; (b) Representative rock-forming minerals assemblages with CGM intergrown with the micas, albite and topaz; (c) Representative rock-forming minerals assemblages with cassiterite replacing the zinnwaldite-lepidolite and development of sericitization of the albite; (d) A representative primary mica of zinnwaldite-lepidolite indistinguishable under optical microscope; (e) SEM-BSE image of the mica in the Fig. 4d showing the relatively dark lepidolite overgrow the bright zinnwaldite along cleavage; (f) SEM-BSE image of a representative mica showing that the relatively dark lepidolite overgrows the bright zinnwaldite, and the darkest secondary muscovite replacing the primary one with irregular boundaries formed and with intergrowth of wolframite, cassiterite and pyrite; (g) Vein type pyrite in the granite with sericitization of feldspar and cassiterite.

4.3. LA-ICP-MS analyses of mica

The trace element analyses of micas were conducted by LA-ICP-MS at the Nanjing FocuMS Techonology Co. Ltd, Nanjing, China. An Analyte Excite 193 nm ArF excimer laser system was connected to an Agilent 7700x ICP-MS instrument to acquire ion-signal intensity. Laser repetition of 7 Hz, energy density of 6 J/cm^2 and spot size of 40 μm were used during the analyses. Helium was applied as carrier gas which was mixed with argon before entering the ICP-MS. Each analysis comprised a background acquisition of approximately 20 s (gas blank) followed by 40 s data acquisition from samples. The NIST SRM 610 was employed as the external standard for trace element calibrations of mica and was analyzed twice every 8–10 sample analyses. The reference materials of BIR-1G, BCR-2G and BHVO-2G served as monitoring standards, and the analytical error was predominantly within 10%. Off-line selection of background and analytical signals, time-drift correction, and quantitative calibration were completed using ICPMSDataCal (Liu et al., 2010).

4.4. LA-MC-ICP-MS sulfur isotope analyses of pyrite

The in-situ sulfur isotope analyses of pyrite were carried out by a Nu Plasma III MC-ICP-MS connected to a RESOlution-155 ArF193-nm laser ablation system at State Key laboratory of Ore Deposit Geochemistry, Institute of Geochemistry, Chinese Academy of Sciences, Guiyang, China. The mass separation was calculated as 0.3333 in the analyses. The instrument was operated in pseudo-medium resolution mode (Millet et al., 2012) to resolve polyatomic interferences from ^{16}O-^{16}O for ^{32}S and ^{16}O-^{18}O for ^{34}S, adjusting the source slit to medium (0.05 mm) in conjunction with using the alpha slit. The pyrite samples were ablated in a mixture of helium (350 ml/min) and nitrogen (2 ml/min) atmosphere using the following parameters: 20 s baseline time, 40 s ablation time, 40 s wash time, 60 μm spot size, 5 Hz repetition rate and 3 J/cm^2 energy density. All analyses followed standard sample bracketing procedures of three samples bracketed by a pyrite pressed powder tablet (PSPT-2) (Bao et al., 2017; Chen et al., 2017). Two in-house standards of natureal pyrite crystals (SB-1 from Shangbao W-Sn deposit and HYC-1 from Huayangchuan Nb-U-REE deposit, China) was analyzed every five unknown samples to monitor the analytical quality. The measured average $\delta^{34}S_{V\text{-}CDT}$ for the standard were 16.55‰ (n = 8) for the SB-1 and −5.62‰ (n = 8) for the HYC-1, which was consistent with the recommended values of 16.57‰ for SB-1 and −5.76‰ for the HYC-1. In this study, the external precision was ca. ± 0.24‰ (2SD).

5. Results

5.1. Whole-rock major and trace element composition

Twenty samples of the three stages of granites from the Limu deposit were selected for major and trace element analyses, including 2 samples for the first stage, 2 samples for the second stage and 16 samples for the third stage, with the results listed in the supplemental Table S1.

The samples of the first and second stages of granites have SiO_2 contents from 73.3 to 74.6 wt%, and the third-stage ones have variable SiO_2 contents from 72.3 to 80.2 wt%. They are all peraluminous with A/CNK ratios from 1.1 to 1.5 (Fig. 5a). The samples of the three stages of granites have low contents of TiO_2 (<0.01 to 0.02 wt%) and MgO (<0.01 to 0.07 wt%), relatively high contents of F (0.2 to 1.3 wt%) and P_2O_5 (0.09 to 0.29 wt%). From the first to the third stage of the granites, the contents of Al_2O_3 and K_2O decrease with increasing SiO_2 content (Fig. 6a, b), and F content is relatively variable, with the third-stage one having the most variable but also the highest values (Fig. 6d).

The granite samples of the three stages show similar flat chondrite-normalized REE patterns, with $(La/Yb)_N$ varying from 0.8 to 6.0, and significant negative Eu anomaly (Eu all below detection limit of 0.03 ppm) (Fig. 5b). However, the concentrations of total rare earth elements (∑REE) decrease significantly from the first and second stage (37.9 to 23.3 ppm) to the third stage (<2.30 ppm) (Fig. 5b). The granite samples are all characterized by enrichments of Rb, Cs, W, Sn and Ta, and depletions of Ba, Sr and Zr in the upper crust-normalized spider diagrams (Fig. 5c), and distinctly low Zr/Hf (5.6 to 18.8) and Nb/Ta (0.4 to 4.2) ratios (supplemental Table S1). From the first-stage to the third-stage granites, the concentrations of Nb (from 24.7 to 149 ppm) and Ta (from 6.6 to 270 ppm) increase with decreasing Nb/Ta ratios (Fig. 6e, f), and concentrations of Sn and W increase, but Zr/Hf ratios decrease (supplemental Table S1).

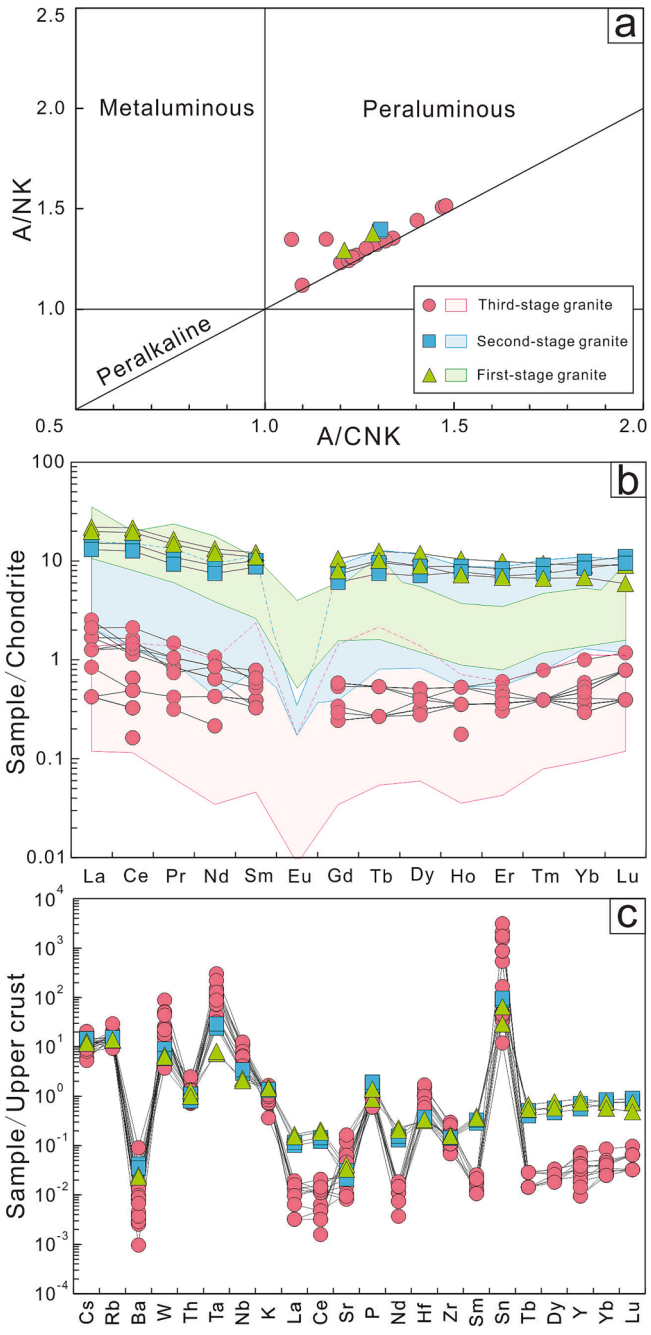

Fig. 5. Bulk chemical diagrams of the three stages of granites at the Limu deposit. (a) A/NK vs. ACNK plot, A = Al_2O_3, C = CaO, N = Na_2O, K = K_2O (in molar proportion); (b) Chondrite-normalized REE patterns, with the shaded areas from Huang et al. (2020) and references therein; (c) Upper crust-normalized trace element diagrams. Chondrite normalization values are from Sun and McDonough (1989), and Upper crust normalization values are from Rudnick and Gao (2003)..

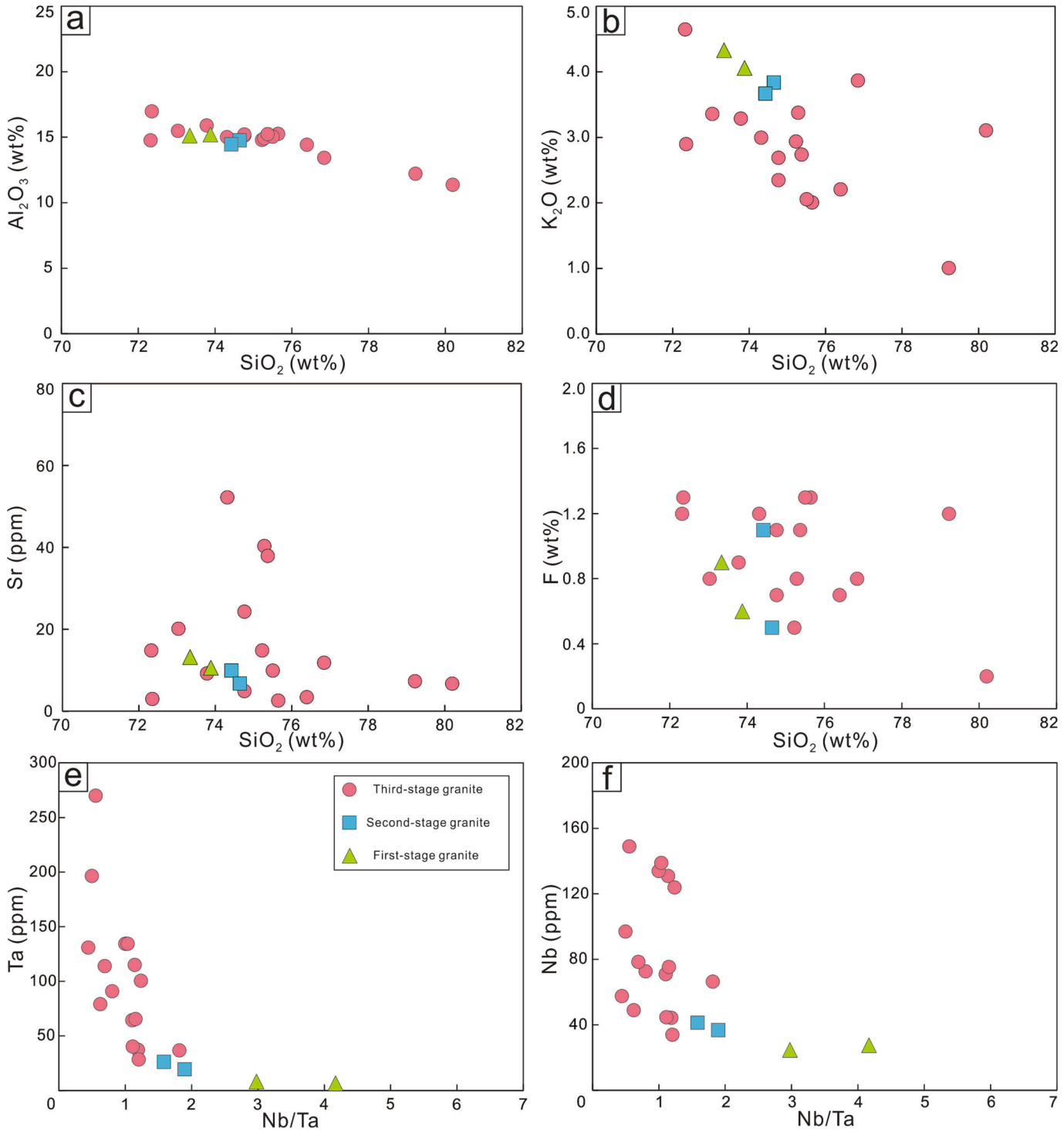

Fig. 6. Bulk chemical diagrams of Al_2O_3 vs. SiO_2 (a), K_2O vs. SiO_2 (b), Sr vs. SiO_2 (c), F vs. SiO_2 (d), Ta vs. Nb/Ta (e), Nb vs. Nb/Ta (f) for the three stages of granites at the Limu deposit.

5.2. Major and trace element concentration of mica

A total of 56 spot analyses by EPMA and LA-ICP-MS have been conducted on micas, where 10 spots were for the first-stage granite, 14 spots for the second-stage granite, and 32 spots for the third-stage granite. The results are summarized in the Table 1 and listed in the supplemental Table S2.

The micas from the first-stage and second-stage granites have largely comparable compositions, that are FeO_{tot} (5.53 to 14.2 wt%), MnO (0.60 to 1.16 wt%), TiO_2 (0.19 to 0.48 wt%), MgO (0.34 to 0.59 wt%), SiO_2 (41.1 to 46.9 wt%), Al_2O_3 (24.0 to 30.9 wt%) and F (3.74 to 6.33 wt%). By comparison, the micas from the former have relatively consistent and higher content ranges of SiO_2 and Al_2O_3, but lower content ranges of FeO, TiO_2 and MgO, corresponding to phengite to Li-phengite (Fig. 7; Table 1), and the micas from the latter have more variable but opposite trends for the content ranges of these elements, corresponding to Li-phengite (Fig. 7). The micas from the third-stage granites fall into two groups of trioctahedral and dioctahedral micas. The principal

Table 1
Concentration and concentration ratio of selective elements of micas from the three stages of granites in Limu deposit.

Granite stage	First-stage granite			Second-stage granite			Third-stage granite								
Mica type	Primary (Li-) phengite			Primary Li-phengite			Primary zinnwaldite			Primary lepidolite			Secondary Li-phengite		
Value	Max.	Min.	Avg.	Max.	Min.	Avg.	Max.	Min.	Avg.	Max.	Min.	Avg.	Max.	Min.	Avg.
SiO_2 (wt%)	46.9	45.9	46.4	46.8	41.1	44.0	47.0	42.9	44.5	53.6	47.8	51.0	52.5	46.3	49.0
TiO_2 (wt%)	0.37	0.19	0.29	0.48	0.32	0.38	0.45	0.10	0.26	0.32	0.12	0.21	0.46	0.11	0.23
Al_2O_3 (wt%)	30.9	28.7	29.5	27.9	24.0	25.7	23.1	21.2	22.1	21.9	19.0	20.0	32.7	28.6	30.7
FeO (wt%)	7.53	5.53	6.40	14.2	8.30	11.3	14.1	11.5	13.1	10.6	5.98	8.08	8.06	2.11	5.04
MnO (wt%)	1.13	0.68	0.99	1.16	0.60	0.86	1.48	1.07	1.26	1.65	0.27	0.67	1.38	0.17	0.58
MgO (wt%)	0.46	0.34	0.38	0.59	0.38	0.47	0.04	0.00	0.01	0.02	0.01	0.01	0.08	0.01	0.03
K_2O (wt%)	10.1	9.29	9.85	10.2	9.49	9.78	9.77	9.05	9.45	10.5	9.77	10.1	10.4	9.63	10.0
F (wt%)	4.58	3.74	4.21	6.33	4.47	5.39	8.96	6.97	7.88	9.79	8.73	9.27	4.72	1.86	3.09
Li (ppm)	5300	3100	4100	8700	4400	6700	18,000	14,000	15,000	24,000	20,000	22,000	6300	1200	3700
Rb (ppm)	6500	3900	5400	8500	4800	6100	12,000	9000	11,000	13,000	10,000	11,000	7200	4000	5500
Nb (ppm)	470	31	160	310	65	180	170	58	110	84	17	51	78	6.1	35
Sn (ppm)	2,500	400	700	700	370	520	280	100	200	120	59	87	510	280	400
Cs (ppm)	690	310	510	1,300	510	750	1,300	890	1,100	1,100	760	930	860	190	510
Ta (ppm)	88	5.1	38	98	13	61	280	88	170	130	11	63	51	13	31
W (ppm)	160	22	73	120	35	81	79	35	58	50	6.2	27	56	4.3	29
Nb/Ta	6.47	2.76	4.42	5.67	0.92	3.50	0.93	0.43	0.66	1.52	0.50	0.98	2.86	0.21	1.32

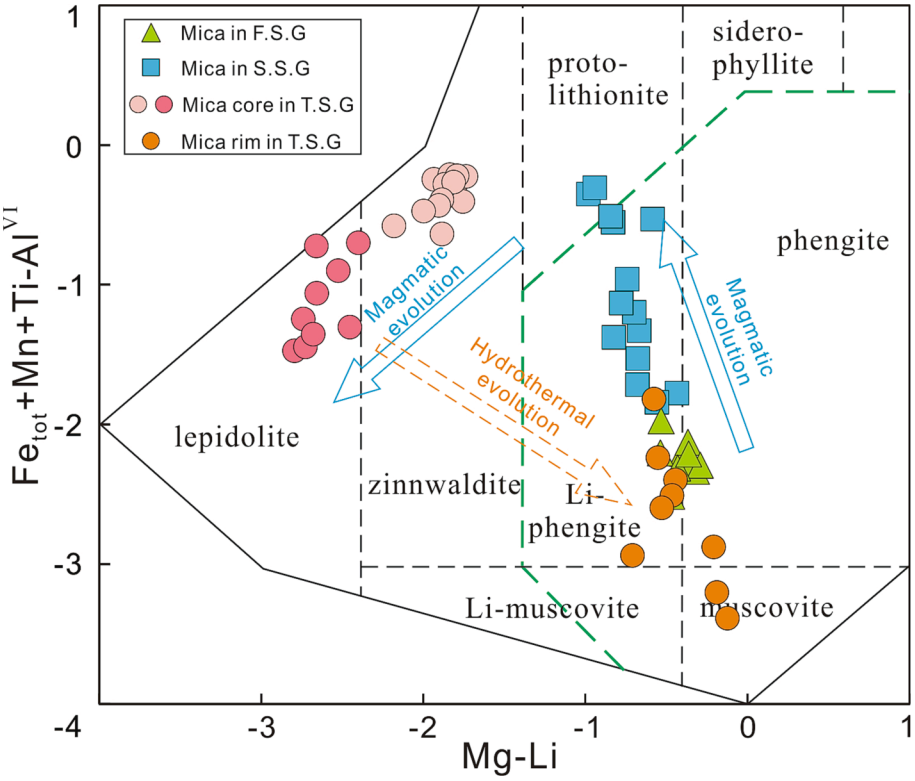

Fig. 7. Classification diagram of micas in the three stages of granites at the Limu deposit, after Tischendorf et al. (1997), with the green dotted line marking the boundary between trioctahedral and dioctahedral micas. The blue solid arrows indicate the magmatic evolution trends of primary micas from the three stages of granites, and the orange dotted arrow indicates the hydrothermal evolution of micas from the lepidolite to the Li-phengite and muscovite in the third-stage granite. F.S.G = first-stage granite; S.S.G = second-stage granite; T.S.G = third-stage granite. (For interpretation of the references to color in this figure legend, the reader is referred to the web version of this article.)

trioctahedral group is the micas that can occur as individual euhedral crystals with planar boundaries with K-feldspar, plagioclase and quartz (Fig. 4b-f). The trioctahedral group has FeO_{tot} (5.98 to 14.1 wt%), MnO (0.27 to 1.65 wt%), TiO_2 (0.10 to 0.45 wt%), MgO (<0.01 to 0.04 wt%), SiO_2 (42.9 to 53.6 wt%), Al_2O_3 (19.0 to 23.1 wt%) and F (6.97 to 9.79 wt %), corresponding to zinnwaldite to lepidolite in composition (Fig. 7; 8a). The dioctahedral group texturally replacing the trioctahedral group (Fig. 4f), by comparison, has higher Al_2O_3 (28.6 to 32.7 wt%) and lower FeO_{tot} (2.11 to 8.06 wt%) and F (1.86 to 4.72 wt%) contents, corresponding to Li-phengite to muscovite in composition (Fig. 7; 8a).

For trace elements, the Li-phengite and phengite from the first-stage and second-stage granites have Li concentrations ranging from 3100 to 8700 ppm, and Rb (3900 to 8500 ppm), Cs (310 to 1300 ppm), Nb (32 to 470 ppm), Ta (5.1 to 98 ppm), Sn (370 to 2500 ppm) and W (22 to 160 ppm), which generally increase with increasing Li concentration (Fig. 8b-e, g, h). By comparison, the euhedral zinnwaldite to lepidolite from the third-stage granites have higher Li concentrations ranging from 14,000 to 24000 ppm, and show higher Rb (9000 to 13000 ppm) and Cs (760 to 1300 ppm) contents, and relatively lower Nb (17 to 170 ppm), Sn (59 to 280 ppm) and W (6.0 to 79 ppm) abundances, and variable but higher Ta (11 to 280 ppm, 130 ppm in average) contents. Except for Rb showing positive correlation, other elements are negatively correlated with the Li concentration (Fig. 8b-e, g, h). The Li-phengite and muscovite texturally replacing zinnwaldite and lepidolite in the third-stage granite are more comparable with the micas from the first- and second-stage granites, which have lower Li (1200 to 6300 ppm), Rb (4000 to 7200 ppm), Cs (190 to 860 ppm), Nb (6.0 to 78 ppm), Ta (13 to 51 ppm) and W (4.0 to 56 ppm), and higher Sn (280 to 510 ppm)

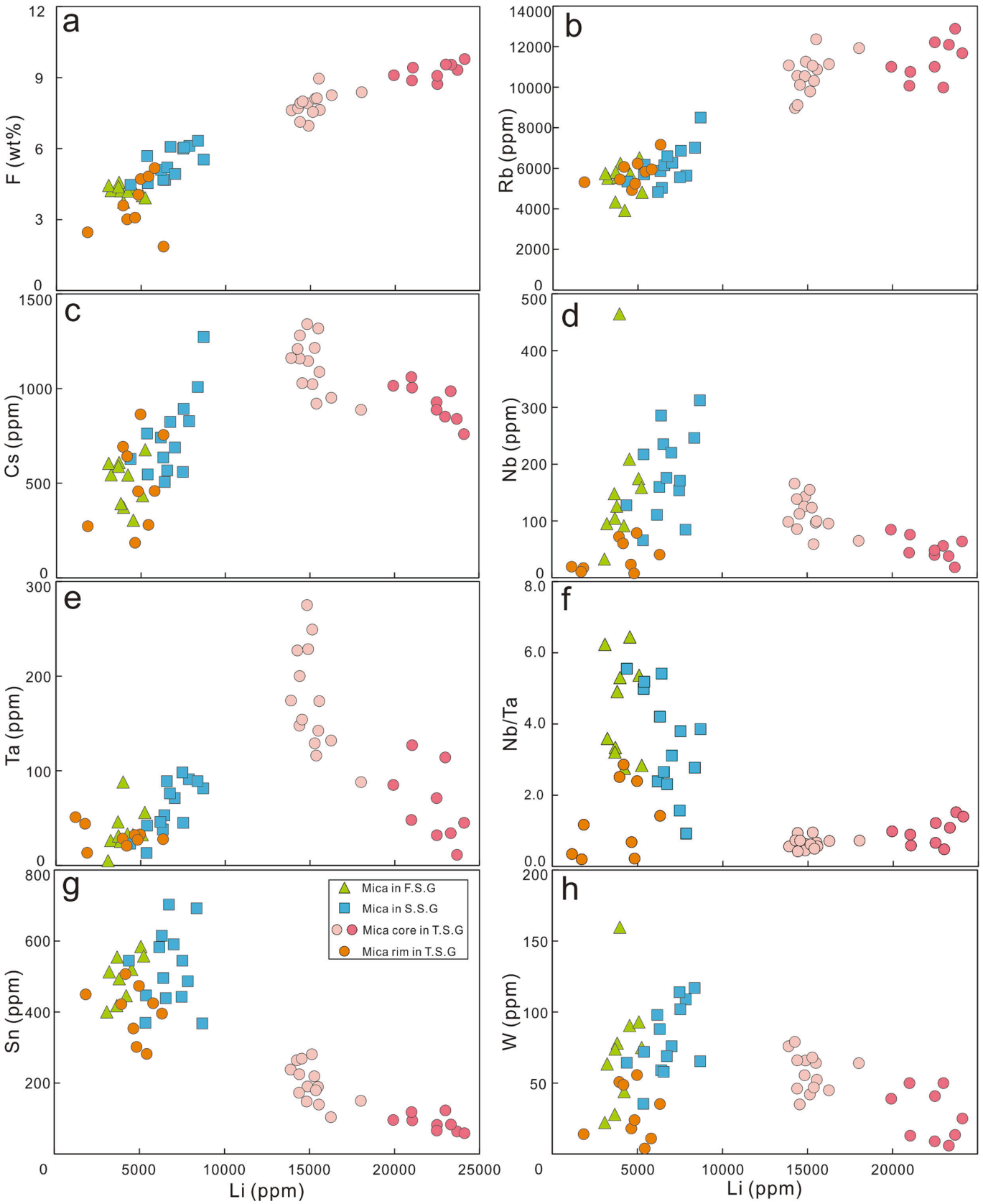

Fig. 8. Chemical diagrams of F (a), Rb (b), Cs (c), Nb (d), Ta (e), Nb/Ta (f), Sn (g), W (h) plotting against Li for micas in the three stages of granites at the Limu deposit. F.S.G = first-stage granite; S.S.G = second-stage granite; T.S.G = third-stage granite.

concentrations than the zinnwaldite and lepidolite.

5.3. Sulfur isotope of pyrite

Sulfur isotopes of the disseminated pyrite and vein-type pyrite in the granite have been obtained by LA-MC-ICP-MS, with the results listed in the supplemental Table S3. The disseminated pyrite crystals have $\delta^{34}S$ ranging from −1.02 to 1.65‰, with an average of 0.71‰ (11 spots), and the vein-type pyrite crystals have $\delta^{34}S$ varying from −0.15 to 2.42‰, with a mean value of 1.12‰ (14 spots).

6. Discussion

6.1. Primary magmatic micas and magma evolution

The three stages of granites at Limu have similar geochemical features, that are peraluminous with relatively high A/CNK ratios, relatively rich in SiO_2, P_2O_5, Rb, Cs, and depleted in Ba and Sr (Fig. 5a, c; supplemental Table S1). Although the third-stage granite samples show relatively large content range of SiO_2, K_2O, Al_2O_3, the principal data correlate well with those of the first- and second-stage granites (Al_2O_3 vs. SiO_2; K_2O vs. SiO_2; Sr vs. SiO_2; Fig. 6a-c). Besides, the three stages of granites were revealed to be consecutive in crystallization age, and consistent in Nd-Hf isotopes, indicating the same magma source from the Proterozoic basement rocks (Feng et al., 2019; Huang et al., 2020). These chemical correlations suggest that the three stages of granite have a genetic linkage. From the first- to the third-stage granites, the total REE concentration decreases successively (Fig. 5b), which is likely attributed to fractional crystallization of REE-rich minerals such as zircon and apatite. The more pronounced negative Eu anomalies combined with stronger depletions of Sr and Ba (Fig. 5b, c) suggest important fractional crystallization of feldspars (plagioclase and K-feldspar; Nash and Crecraft, 1985). The notable Nb and Ta enrichments during the magma evolution (Fig. 6e, f) can be ascribed to their incompatibility in feldspars and quartz (Nash and Crecraft, 1985), however, the simultaneous decrease of Nb/Ta ratios likely points to a critical role of fractional crystallization of micas, because of its preferentially incorporating Nb relative to Ta (Stepanov and Hermann, 2013; Stepanov et al., 2014). Collectively, these successive chemical variations conform to typical chemical differentiation trends of magma caused by fractional crystallization, and further suggest that the three stages of granites were likely a result of successive magma evolution from a shallow magma chamber, rather than three individual magma batches from the same source. Besides, the Nb/Ta and Zr/Hf ratios (Fig. 6e, f; supplemental Table S1) decrease continuously, and contents of F increase as a whole (Fig. 6d), which all indicate that the Limu granite complex is increasingly evolved from the first- to the third-stage granite.

The micas in the first- and second-stage granites and the majority of micas (trioctahedral group) in the third-stage granite all are relatively euhedral crystals, and exhibit planar boundaries with other igneous minerals (plagioclase, K-feldpsar and quartz) (Fig. 3b, e; 4b-e). These textural features conform to equilibrium igneous texture, suggesting that these micas are primary magmatic micas. These primary micas show a wide range of composition, that evolve from phengite to Li-phengite for the first to second stages of granites, and from zinnwaldite to lepidolite for the third-stage granite based on the classification proposed by Tischendorf et al. (1997) (Fig. 7). These evolutions are consistent with typical compositional trends of dioctahedral and trioctahedral micas under magmatic evolution (e.g., Cuney et al., 1992; Tischendorf et al., 1997; Van Lichtervelde et al., 2008; Li et al., 2015, 2021). The concentrations of Li, F, Rb and Cs of micas increase continuously with the mica evolutions (Fig. 8a-c), which are likely correlated with the following substitution reactions: (1) F → OH; (2) Li + Al^{VI} → Fe + Mg; (3) (Rb, Cs) → (K, Na) (e.g., Robert et al., 1993; Pesquera et al., 1999; Černý et al., 2003). Noticeably, for the primary micas from the first-stage to the third-stage granites, the K/Rb and K/Cs ratios decrease exponentially with the increasing Rb and Cs concentrations (Fig. 9a, b). Such correlations conform to typical chemical trends of micas with magma evolution of cogenetic system (Černý et al., 1985; Roda-Robles et al. 2012; Hulsbosch et al., 2014; Marchal et al. 2014; Han et al., 2021), and are indicative of fractional crystallization of feldspar and micas in the process (London, 2022). Lithium and F are flux components generally concentrated in late-stage residual melts, which are incompatible with feldspar and quartz, but compatible with micas. Rubidium and Cs are incompatible with plagioclase and quartz but relatively compatible with K-feldspar and micas. Thus, the continuous increases of the abundances of these elements in micas (Fig. 8a-c) suggest a fractional crystallization process dominated by feldspar (particularly plagioclase) and quartz, with minor amount of mica. The fractional crystallization processes mainly occurred in the magma chamber level, which controlled the magma and mica evolution of the three stages of granites. Nevertheless, the magmatic mica evolution from zinnwaldite to lepidolite within the third-stage granite likely occurred during emplacement and in-situ fractional crystallization of the magma.

The Nb and Ta contents of the Li-phengites from first- to the second-stage granites increase with evolution (Fig. 8d, e), suggesting that the fractional crystallized minerals are dominated by feldspar and/or quartz, which are highly incompatible with Nb and Ta. In addition, the Nb/Ta ratios decrease slightly (Avg. 4.4 to 3.5; Fig. 8f), which is consistent with bulk chemical evolution trends of the granites (Fig. 6e, f). Noticeably, from zinnwaldite to lepidolite in the third-stage granite, the Nb and Ta concentration decrease (Fig. 8d, e) and Nb/Ta ratios increase slightly (Avg. 0.66 to 0.98; Fig. 8f). Such chemical evolutions of micas are opposite to the bulk chemical evolution trends of the granite that increase in Ta and Nb concentrations with decreasing Nb/Ta ratios. Thus, the Nb-Ta evolution trends of the micas were not related to bulk chemical evolution of the granite. Instead, the decreasing concentration of Nb and Ta of the micas was likely caused by co-crystallization of minerals much more compatible with Nb and Ta than mica, for which Ti-rich minerals (rutile, ilmenite and titanite) and Ta-Nb oxides are best candidates (Stepanov et al., 2014). The third-stage granite is distinctly Ti-depleted, but is Ta-Nb mineralized occurring as CGM, suggesting that co-crystallization of CGM is the key reason for the decreasing Ta and Nb concentrations of micas. The markedly lower Nb concentration and Nb/Ta ratios of zinnwaldite (avg. 0.66) compared to the Li-phengite from the second-stage granite (avg. 3.5) suggest that crystallization of CGM occurred at early sub-stage in the third-stage granite. In addition, the CGM was much enriched in Nb relative to Ta to account for the preceding decrease of Nb and marked low Nb/Ta ratios of the zinnwaldite. Then, the increasing Nb/Ta ratios from zinnwaldite to lepidolite are likely related to evolution of CGM toward Ta enrichment, which commonly happens in granites and pegmatites worldwide (Černý et al., 1985, 1986; Van Lichtervelde et al., 2007; Wu et al., 2018). To sum up, the content variations of Nb and Ta of the primary micas (zinnwaldite to lepidolite) in the third-stage granite record crystallization and Ta-Nb fractionation of CGM, and further suggest that magmatic processes are critical in the Ta-Nb mineralization at Limu.

Similarly, the increase of W and Sn concentrations of the Li-phengites from the first- to second-stage granites is attributed to their incompatibility with the dominant fractional crystallized minerals of feldspar and quartz in magma evolution. It is noted that the primary micas in the third-stage granite are lower in Sn and W concentration than the primary Li-phengite in the second-stage granite (Fig. 8g, h). These decreases of Sn and W concentrations of micas are not likely attributed to crystallizations of magmatic cassiterite and wolframite in the third-stage granite, because cassiterite and wolframite therein replace the primary micas (Fig. 4c, f) and are no doubt secondary in origin. The CGM can incorporate considerable W and Sn, and that from third-stage granites has higher contents of W than Sn (average 11.6 wt% vs. 3.1 wt% in Ma (2019)). If the crystallization of CGM is the dominant reason for the decreasing W and Sn concentration of the primary micas, the decrease of W concentration should be more notable than the Sn

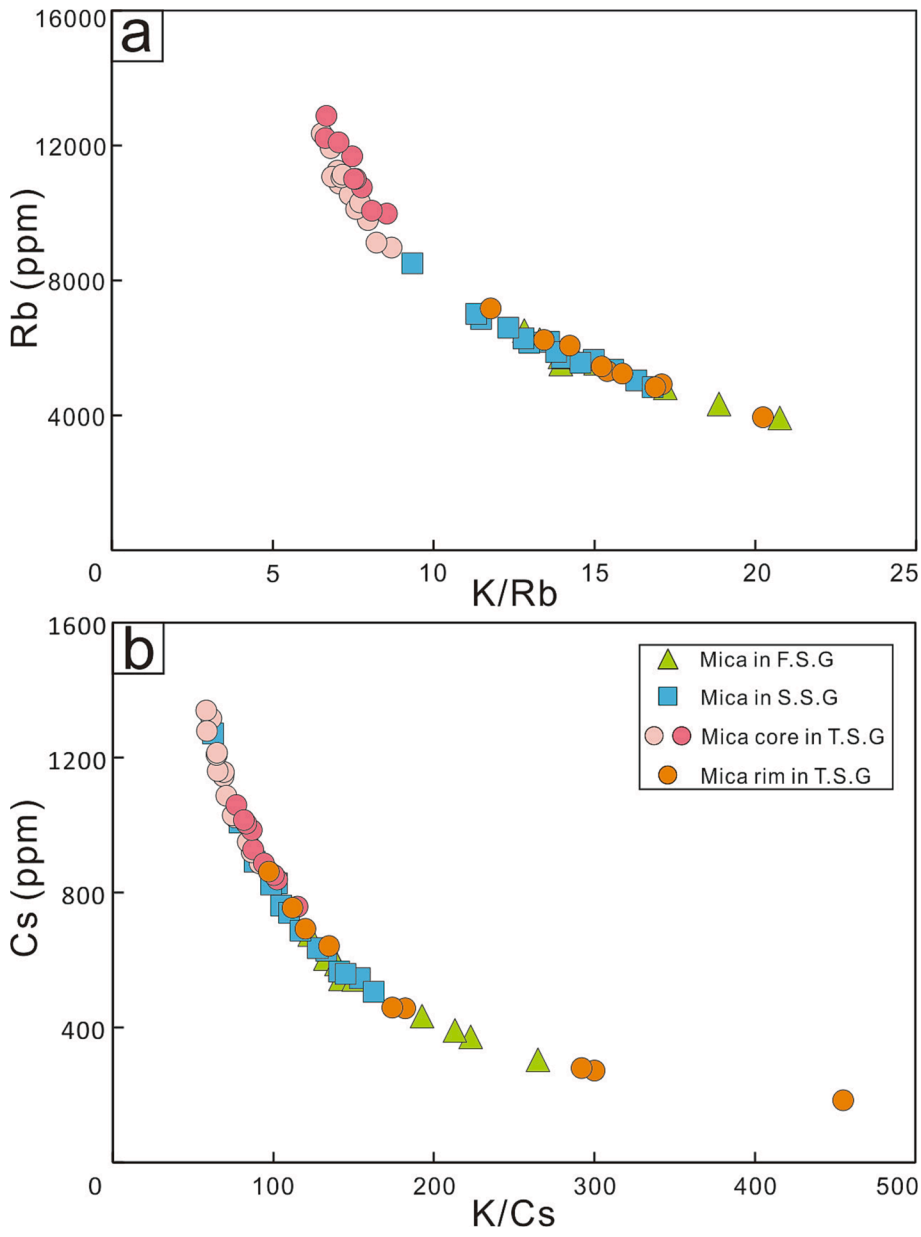

Fig. 9. Diagrams of Rb vs. K/Rb (a), Cs vs. K/Cs (b) for micas in the three stages of granites at the Limu deposit. F.S.G = first-stage granite; S.S.G = second-stage granite; T.S.G = third-stage granite.

concentration, which is opposite to the data (Table 1; Fig. 8g, h). Besides, a decrease of mica/melt partition coefficients of Sn (4.14 to 2.32) and W (10.71 to 0.4) with the mica changing from muscovite to biotite might be a possible cause (Simons et al., 2017). If so, the decrease of W concentration would be also expected to be more marked than the Sn concentration, which is opposite to the facts (Table 1; Fig. 8g, h). Thus, we argue that the decreasing W and Sn concentrations in the primary micas of the third-stage granite are likely ascribed to that W and Sn in the magma largely concentrated in the volatile (H_2O and/or Cl) and flux (Li and F) components, as the third-stage granite is flux-rich and developed with hydrothermal W-Sn mineralization (rich in volatiles).

6.2. *Secondary hydrothermal micas and fluid source*

In the third-stage granite at Limu, secondary mica is developed after the zinnwaldite and lepidolite. Texturally, it replaces the primary zinnwaldite-lepidolite as mica rim with relatively irregular boundaries cutting the cleavage of primary ones (Fig. 4f), which is distinguishable from magmatic textures. Paragenetically, it occurs after the lepidolite and is synchronous with cassiterite, wolframite and pyrite (Fig. 4f). Critically, cassiterite and wolframite also replace the primary zinnwaldite-lepidolite and overgrow CGM, and are closely coexisting with secondary sericitization of feldspars and vein-type pyrite in the granite (Fig. 4c, f, g), evidently suggesting their hydrothermal origin. Chemically, the secondary mica is Li-phengite based on the classification proposed by Tischendorf et al. (1997). The evolution from zinnwaldite-lepidolite to Li-phengite (Fig. 7) is inconsistent with magmatic mica evolution trend. In addition, compared to the primary zinnwaldite-lepidolite, it is distinctly depleted in Li, Rb, Cs and F with higher K/Rb and K/Cs ratios (Fig. 8a-c; 9a, b), which are also opposite to chemical evolution trends of micas with magma evolutions (e.g., Černý et al., 1985; Roda-Robles et al. 2012; Hulsbosch et al., 2014; Marchal et al. 2014; London, 2022). Moreover, the secondary Li-phengite has elevated Sn and/or W concentrations compared to the primary lepidolite (Fig. 8g, h), which are elements preferentially partitioning into hydrothermal fluids relative to melts (Zajacz et al., 2008; Audétat and Edmonds,

2020). Besides, the third-stage granite exhibits relatively wide ranges of SiO_2, K_2O and F with occurrences of abnormally high SiO_2 (greater than76 wt%) and low K_2O (<2.5 wt%) and F contents, likely indicating chemical modification from subsolidus hydrothermal processes occurred in the granite. Collectively, these lines of evidence all suggest that the secondary Li-phengite in the third-stage granite has a hydrothermal origin, and likely formed by recrystallization from the primary micas via replacing reaction under subsolidus condition.

Such secondary hydrothermal micas depleted in Li, F, Rb and Cs are not uncommon in rare metal-W-Sn mineralized granite and pegmatites, such as Yashan (Li et al., 2015), Dahutang (Yin et al., 2019) and Xihuashan (Li et al., 2021) in South China, and Zhaojinggou (Wei et al., 2020) in North China. Regarding the depletion of Li, F, Rb and Cs in the secondary hydrothermal micas, some studies proposed that it might be attributed to a dominant involvement of external fluids in hydrothermal systems (Li et al., 2015, 2021). However, in the third-stage granite at Limu, the disseminated and vein-type pyrite have consistent $\delta^{34}S$ values of 0.71‰ and 1.12‰ (supplemental Table S3), which are in accordance with magmatic sulfur (Ohmoto 1972; Seal 2006). The pyrite is synchronous with the secondary Li-phengite and the cassiterite and wolframite in the third-stage granite insight from their textural intergrowth (Fig. 4f, g). In addition, the development of disseminated pyrite to vein-type pyrite is likely reflective of concentration of hydrothermal fluids in the post-magmatic stage. If massive external fluids were involved in the post-magmatic hydrothermal system, exotic sulfur and redox changes would be accompanied to cause significant variations of the pyrite $\delta^{34}S$ values (Ohmoto 1972; Seal 2006). Hence, the consistent $\delta^{34}S$ values of pyrite suggest that the hydrothermal fluids accounting for the secondary Li-phengite were dominantly magmatic fluids without notable involvement of external fluids.

Lithium, F, Rb and Cs are all typical fluid-mobile elements. London (2022) summarized that the depletion of Rb and Cs and higher K/Rb and K/Cs ratios in secondary feldspars and micas from pegmatites and granites were due to recrystallization of these minerals in open hydrothermal systems and loss of Rb and Cs into fluids. In the third-stage granite of Limu, fluorite-lepidolite veinlets are developed in overlying sedimentary country rocks, which evidently suggest that the post-magmatic fluids were not depleted in F and Li. Instead, similar to the processes proposed by London (2022), the secondary Li-phengite likely recrystallized via replacing the primary zinnwaldite and lepidolite in an open hydrothermal system, and F and Li as well as Rb and Cs concentrated in fluid and migrated away with exsolved fluids to cause the depletions of Li, F, Rb and Cs of the Li-phengite.

6.3. *Implications for Ta-Nb-Sn-W mineralization*

The Limu is a Ta-Nb-Sn-W polymetallic deposit. The Ta, Nb, Sn and W are all highly incompatible elements in melt system, and therefore mineralization of these elements in granites definitely requires high degrees of magma differentiation. In the Limu deposit, only the third-stage granite is Ta-Nb mineralized with considerable reserves, and the second and third stages are both Sn-W mineralized. Meanwhile, the granite complex is more and more evolved in composition from the first- to the third-stage granite, indicated by the decreasing Nb/Ta and Zr/Hf ratios in particular (Fig. 6e, f; supplemental Table S1). Thus, it can be inferred that the Ta-Nb mineralization requires a higher degree of magmatic differentiation than the Sn-W mineralization. Noticeably, the Li content of micas increase significantly from the first- to the third-stage granite, with the most Ta-Nb enriched third-stage granite developed with Li-rich mica of zinnwaldite to lepidolite. Similarly, in the Nanling Range, the Ta-Nb mineralized granites are also characterized by occurrences of zinnwaldite to lepidolite, like Yashan (Yichun; Li et al., 2015), Jianfengling (Diao et al., 2022) and Laiziling (Xie et al., 2018), which are more enriched in Li than those micas from granites that are W-Sn mineralized with relatively insignificant Ta-Nb mineralization (Fig. 10), like Piaotang (Legros et al., 2018), Xihuashan (Li et al., 2021)

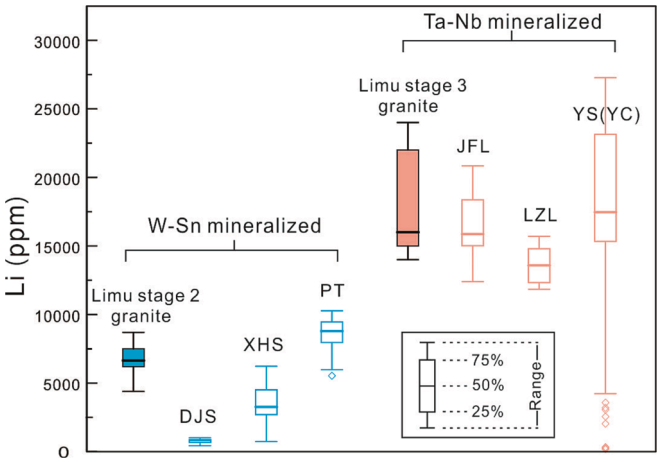

Fig. 10. Comparison of Li contents in primary micas from Ta-Nb mineralized and W-Sn mineralized granites, Nanling Range. JFL = Jianfengling; LZL = Laiziling; YS (YC) = Yashan (Yichun); DJS = Dajishan; XHS = Xihuashan; PT = Piaotang.

and Dajishan (Wu et al., 2017). Thus, occurrences of highly Li-enriched micas (zinnwaldite and lepidolite) in granites can likely exert a mineralogical indicator of Ta-Nb mineralization, which may have potentials to be applied to granites and pegmatites worldwide.

As discussed in the section 6.1, magmatic processes played a critical role in Ta-Nb enrichments and mineralization at Limu, which is also commonly agreed for Ta-Nb mineralization in granites and pegmatites worldwide (Linnen et al. 2012). The fractional crystalized minerals in the magma evolution of the granite complex at Limu were dominated by feldspars and quartz, which are incompatible with Ta and Nb (Stepanov et al., 2014, and references therein), and therefore, the fractional crystallization processes could contribute to concentration and saturation of Ta and Nb in the latest stage granite. Although the proportion of micas in the fractional crystallized minerals was relatively small, it also played a critical role in the Ta-Nb mineralization. On one hand, micas incorporated Ti and suppressed crystallization of Ti-bearing minerals (rutile, ilmenite and titanite) to prevent loss of Ta and Nb at early stage of magma differentiation, because Ta and Nb strongly partition into these Ti-bearing minerals (Stepanov and Herman, 2013; Stepanov et al., 2014). This effect can be seen from the distinct depletion of Ti in the granites and the TiO_2 contents in the micas (Table 1; supplemental Table S1, S2). On the other hand, fractional crystallization of micas fractionated Ta from Nb due to its preferential incorporation of Nb relative to Ta (Stepanov et al., 2014), which contributed to Ta enrichment and mineralization in the latest stage of granite. This role can be confirmed by the higher concentration of Nb than Ta and Nb/Ta ratios larger than 1 of the primary Li-phengite in the first- and second-stage of granites. With the magma evolution, flux and volatile components of Li, F and H_2O are enriched in the latest stage as indicated by the chemical features of the primary micas from the three stages of granites (Table 1). These flux enrichments could increase Ta-Nb solubility of magma, and significantly reduce the crystallization temperature of magma to finally trigger saturation and crystallization of Ta-Nb oxides (Linnen et al. 1998; Bartels et al. 2010; Fiege et al. 2011), which would increase Ta-Nb resource potential of granites. A hydrothermal process in the third-stage granite was identified by secondary mica rim. Noticeably, compared to the primary zinnwaldite-lepidolite, the lower Ta and Nb concentrations of the hydrothermal Li-phengite (Fig. 8d, e) suggest that at least small amounts of Ta and Nb in the primary micas were transferred by the fluid during the replacing and recrystallizing processes. Such Ta-Nb mobility was likely related to F-rich and relatively low-pH hydrothermal conditions, where solubilities of Ta and Nb are relatively high (Timofeev et al. 2015, 2017; Akinfiev et al. 2020). However, the potential role of

hydrothermal processes in contributing to Ta-Nb resources would depend on whether the transferred Ta-Nb can effectively reconcentrate to precipitate Ta-Nb oxides, which requires further direct mineralogical evaluation from Ta-Nb oxides.

Similarly, Sn and W are also incompatible with the dominant fractional crystallized minerals and therefore concentrate with the magma evolution at Limu (supplemental Table S1). The enrichments of flux components could also contribute to the enrichments of Sn and W (Linnen, 1998; Bhalla et al., 2005), and in the flux-rich third-stage granitic magma, Sn and W likely concentrated in the volatile and flux components. Although it seems to be possible that wolframite crystallizes from melts (e.g., Che et al., 2013), the cassiterite and wolframite in the third-stage granite of Limu are no doubt hydrothermal in origin as is evidenced by textural features (Fig. 4c, f, g). The hydrothermal fluids related to the secondary mica and cassiterite and wolframite in the granite were revealed to be dominated by magmatic fluids, and thereby, fluid mixing (between post-magmatic fluids and external fluids) was not the precipitation mechanism for the cassiterite and wolframite. The Sn-W-rich hydrothermal fluids were likely saturated at post-magmatic stage to interact with the crystallized feldspar and micas under a sub-solidus condition. These interactions are H^+ consumed and would lead to a pH increase of fluid, which eventually contributed to precipitations of cassiterite and wolframite in the granite (e.g., Heinrich, 1990; Wood and Samson, 2000; Lehmann, 2021). Noticeably, quartz vein type W-Sn mineralization is also developed in overlying country rocks. Such mineralization suggests that a large portion of W and Sn in fluids did not precipitate in the granite roof but migrated away with exsolved fluids and ultimately precipitated.

7. Conclusions

(1) Granite and mica chemistry reveals that the three stages of granites at the Limu deposit were genetically linked. The micas are increasingly enriched in Li, F, Rb and Cs with decreasing K/Rb and K/Cs ratios, suggesting a dominant fractional crystallization of feldspars, particularly plagioclase, with minor micas in the magma evolution.
(2) Variations of Ta and Nb concentration and Nb/Ta ratios of micas indicate that magmatic processes played a critical role in Ta-Nb mineralization of the Limu deposit. The CGM crystallized at the early sub-stage of the third-stage granitic magma, and occurred with fractionation of Ta from Nb with magma evolution.
(3) Secondary hydrothermal micas distinctly depleted in Li, F, Rb and Cs occur after the primary zinnwaldite-lepidolite in the third-stage granite. The consistent $\delta^{34}S$ values close to 0‰ of pyrite indicate that the hydrothermal system was dominated by magmatic fluids. The lower Ta-Nb concentrations in the hydrothermal micas suggest that at least small amounts of Ta and Nb were transferred by the fluid.
(4) The Sn and W likely concentrated in the volatile and flux components in the third-stage magma, and cassiterite and wolframite in the granite are hydrothermal and precipitated by fluid-rock interaction. A portion of W and Sn migrated away with exsolved fluids and formed the quartz vein W-Sn mineralization.

Declaration of Competing Interest

The authors declare that they have no known competing financial interests or personal relationships that could have appeared to influence the work reported in this paper.

Data availability

Data will be made available on request.

Acknowledgements

We thank Yun-Tong Liu, Jian-Ping Liu and Dan Chen for their helps in field works, EPMA analyses and LA-MC-ICP-MS sulfur isotope analyses, respectively. This study was financially supported by the National Key Research and Development Program of China (Grant No. 2018YFA0702603; 2017YFC0602402), the West Light Foundation of The Chinese Academy of Sciences (Grant No. xbzg-zdsys-202108) and the Special Fund of the State Key Laboratory of Ore Deposit Geochemistry (202301).

Appendix A. Supplementary data

Supplementary data to this article can be found online at https://doi.org/10.1016/j.oregeorev.2023.105584.

References

Akinfiev, N.N., Korzhinskaya, V.S., Kotova, N.P., Redkin, A.F., Zotov, A.V., 2020. Niobium and tantalum in hydrothermal fluids: Thermodynamic description of hydroxide and hydroxofluoride complexes. Geochim. Cosmochim. Acta 280, 102–115.
Anderson, M.O., Lentz, D.R., McFarlane, C.R.M., Falck, H., 2013. A geological, geochemical and textural study of a LCT pegmatite: implications for the magmatic versus metasomatic origin of Nb–Ta mineralization in the Moose II pegmatite, Northwest Territories, Canada. J. Geosci. 58, 299–320.
Audétat, A., Edmonds, M., 2020. Magmatic-Hydrothermal Fluids. Elements 16, 401–406.
Bao, Z.A., Chen, L., Zong, C.L., Yuan, H.L., Chen, K.Y., Dai, M.L., 2017. Development of pressed sulfide powder tablets for in situ sulfur and lead isotope measurement using LA-MC-ICP-MS. Int. J. Mass Spectrom. 421, 255–262.
Bartels, A., Holtz, F., Linnen, R.L., 2010. Solubility of manganotantalite and manganocolumbite in pegmatitic melts. Am. Miner. 95 (4), 537–544.
Bhalla, P., Holtz, F., Linnen, R.L., Behrens, H., 2005. Solubility of cassiterite in evolved granitic melts: effect of T, fO2, and additional volatiles. Lithos 80 (1-4), 387–400.
Černý, P., Meintzer, R.E., Anderson, A.J., 1985. Extreme fractionation in rare-element granitic pegmatites; selected examples of data and mechanisms. Can. Miner. 23, 381–421.
Černý, P., Goad, B.E., Hawthorne, F.C., Chapman, R., 1986. Fractionation trends of the Nb-and Ta-bearing oxide minerals in the Greer Lake pegmatitic granite and its pegmatite aureole, southeastern Manitoba. Am. Miner. 71, 501–517.
Černý, P., Chapman, R., Teertstra, D.K., Novák, M., 2003. Rubidium- and cesium-dominant micas in granitic pegmatites. Am. Mineral. 88 (11-12), 1832–1835.
Černý, P., Blevin, P.L., Cuney, M., London, D., 2005. Granite-related ore deposits. In: Hedenquist, J.W., Thompson, J.F.H., Goldfarb, R.J., Richards, J.P. (Eds.), Economic Geology—One Hundredth Anniversary Volume, 1905–2005: Littleton. Society of Economic Geologists, Colo., pp. 337–370
Che, X.D., Linnen, R.L., Wang, R.C., Aseri, A., Thibault, Y., 2013. Tungsten solubility in evolved granitic melts: an evaluation of magmatic wolframite. Geochim. Cosmochim. Acta 106, 84–98.
Che, X.D., Wang, R.C., Wu, F.Y., Zhu, Z.Y., Zhang, W.L., Hu, H., Xie, L., Lu, J.J., Zhang, D., 2019. Episodic Nb–Ta mineralisation in South China: Constraints from in situ LA–ICP–MS columbite-tantalite U-Pb dating. Ore Geol. Rev. 105, 71–85.
Chen, J., Wang, R.C., Zhu, J.C., Lu, J.J., Ma, D.S., 2014. Multiple-aged granitoids and related tungsten-tin mineralization in the Nanling Range, South China. Sci. China-Earth Sci. 56, 2045–2055. In Chinese.
Chen, L., Yuan, H.L., Chen, K.Y., Bao, Z.A., Zhu, L.M., Liang, P., 2019. In situ sulfur isotope analysis by laser ablation MC-ICPMS and a case study of the Erlihe Zn-Pb ore deposit, Qinling orogenic belt, Central China. J. Asian Earth Sci. 176, 325–336.
Cuney, M., Marignac, C., Weisbrod, A., 1992. The Beauvoir topaz–lepidolite albite granite (Massif Central, France): the disseminated magmatic Sn–Li–Ta–Nb–Be mineralization. Econ. Geol. 87, 1766–1794.
Diao, X.i., Wu, M., Zhang, D., Liu, J., 2022. Textural features and chemical evolution of Ta-Nb-W-Sn oxides in the Jianfengling Deposit, South China. Ore Geol. Rev. 142, 104690.
Feng, M., Feng, Z., Kang, Z., Fu, W., Qing, Y., Hu, R., Cai, Y., Feng, Y., Wang, C., 2019. Establishing an Indosinian geochronological framework for episodic granitic emplacement and W-Sn-Nb-Ta mineralization in Limu mining district, South China. Ore Geol. Rev. 107, 1–13.
Feng, Z., Kang, Z., Yang, F., Liao, J., Wang, C., 2013. Geochronology of the Limu W-Sn–Nb–Ta-bearing granite pluton in South China. Resour. Geol. 63 (3), 320–329.
Fiege, A., Kirchner, C., Holtz, F., Linnen, R.L., Dziony, W., 2011. Influence of fluorine on the solubility of manganotantalite (MnTa2O6) and manganocolumbite (MnNb2O6) in granitic melts — An experimental study. Lithos 122 (3-4), 165–174.
Han, J., Chen, H., Hollings, P., Wang, J., Zhang, D., Zhang, L.e., Zeng, T.i., Ma, J., Ai, Y., 2021. Efficient enrichment of Rb during the magmatic-hydrothermal transition in a highly evolved granitic system: Implications from mica chemistry of the Tiantangshan Rb-Sn-W deposit. Chem. Geol. 560, 120020.
Heinrich, C.A., 1990. The Chemistry of Hydrothermal Tin(-Tungsten) Ore Deposition. Econ. Geol. 85, 457–481.

Huang, W., Wu, J., Liang, H., Zhang, J., Ren, L., Chen, X., 2020. Ages and genesis of W-Sn and Ta-Nb-Sn-W mineralization associated with the Limu granite complex, Guangxi, China. Lithos 352-353, 105321.
Hulsbosch, N., Hertogen, J., Dewaele, S., André, L., Muchez, P., 2014. Alkali metal and rare earth element evolution of rock-forming minerals from the Gatumba area pegmatites (Rwanda): quantitative assessment of crystal-melt fractionation in the regional zonation of pegmatite groups. Geochim. Cosmochim. Acta 132, 349–374.
Kaeter, D., Barros, R., Menuge, J.F., Chew, D.M., 2018. The magmatic–hydrothermal transition in rare-element pegmatites from southeast Ireland: LA-ICP-MS chemical mapping of muscovite and columbite–tantalite. Geochim. Cosmochim. Acta 240, 98–130.
Legros, H., Marignac, C., Tabary, T., Mercadier, J., Richard, A., Cuney, M., Wang, R.C., Charles, N., Lespinasse, M.Y., 2018. The ore-forming magmatic-hydrothermal system of the Piaotang W-Sn deposit (Jiangxi, China) as seen from Li-mica geochemistry. Am. Mineral. 103, 39–54.
Lehmann, B., 2021. Formation of tin ore deposits: A reassessment. Lithos 402-403, 105756.
Li, J., Huang, X.L., He, P.L., Li, W.X., Yu, Y., Chen, L.l., 2015. In situ analyses of micas in the Yashan granite, South China: Constraints on magmatic and hydrothermal evolutions of W and Ta–Nb bearing granites. Ore Geol. Rev. 65, 793–810.
Li, J., Huang, X.L., Fu, Q., Li, W.X., 2021. Tungsten mineralization during the evolution of a magmatic-hydrothermal system: Mineralogical evidence from the Xihuashan rare-metal granite in South China. Am. Mineral. 106, 443–460.
Li, Z.X., Li, X.H., 2007. Formation of the 1300 km-wide intra-continental orogen and post orogenic magmatic province in Mesozoic South China: a flat-slab subduction model. Geology 35, 179–182.
Linnen, R.L., 1998. The Solubility of Nb-Ta-Zr-Hf-W in Granitic Melts with Li and Li + F: Constraints for Mineralization in Rare Metal Granites and Pegmatite. Econ. Geol. 93, 1013–1025.
Linnen, R.L., Cuney, M., 2005. Granite-related rare-element deposits and experimental constraints on Ta-Nb-W-Sn-Zr-Hf mineralization. in: Linnen, R. L. and Samson, I. M., (Eds.), Rare-Element Geochemistry and Mineral Deposits. Geological Association of Canada Short Course Notes, St. John's, NL, Canada, pp. 45-68.
Linnen, R.L., Van Lichtervelde, M., Cerny, P., 2012. Granitic pegmatites as sources of strategic metals. Elements 8 (4), 275–280.
Liu, YongSheng, Hu, ZhaoChu, Zong, KeQing, Gao, ChangGui, Gao, S., Xu, J., Chen, HaiHong, 2010. Reappraisement and refinement of zircon U-Pb isotope and trace element analyses by LA-ICP-MS. Chin. Sci. Bull. 55 (15), 1535–1546.
London, D., 2022. A Rayleigh model of cesium fractionation in granite-pegmatite systems. Am. Mineral. 107, 82–91.
Ma, W.W., Huang, X.L., Yu, Y., Yin, R., He, P.L., 2020. Characteristics of Micas in the Limu Granites, South China: An Indicator of the Hydrothermal Processes Related to Tin Mineralization. Geotecton. Metallog. 44, 1143–1159 in Chinese with English abstract.
Mao, J.W., Cheng, Y.B., Chen, M.H., Pirajno, F., 2013. Major types and time–space distribution of Mesozoic ore deposits in South China and their geodynamic settings. Miner. Deposita 48, 267–294.
Marchal, K.L., Simmons, W.B., Falster, A.U., Webber, K.L., Roda-Robles, E., 2014. Geochemistry, mineralogy, and evolution of Li–Al micas and feldspars from the Mount mica pegmatite, Maine, USA. Can. Mineral. 52 (2), 221–233.
Melcher, F., Graupner, T., Gäbler, H., Sitnikova, M., Oberthür, T., Gerdes, A., Badanina, E., Chudy, T., 2017. Mineralogical and chemical evolution of tantalum–(niobium–tin) mineralisation in pegmatites and granites. Part 2: Worldwide examples (excluding Africa) and an overview of global metallogenetic patterns. Ore Geol. Rev. 89, 946–987.
Michaud, J.A.S., Pichavant, M., 2020. Magmatic fractionation and the magmatic-hydrothermal transition in rare metal granites: Evidence from Argemela (Central Portugal). Geochim. Cosmochim. Acta 289, 130–157.
Millet, M.A., Baker, J.A., Payne, C.E., 2012. Ultra-precise stable Fe isotope measurements by high resolution multiple-collector inductively coupled plasma mass spectrometry with a 57Fe–58Fe double spike. Chem. Geol. 304–305, 18–25.
Nash, W.P., Crecraft, H.R., 1985. Partition coefficients for trace elements in silicic magmas. Geochim. Cosmochim. Acta 49 (11), 2309–2322.
Ohmoto, H., 1972. Systematics of sulfur and carbon isotopes in hydrothermal ore deposits. Econ. Geol. 67, 551–578.
Pesquera, A., Torres Ruiz, J., Gil Crespo, P.P., Velilla, N., 1999. Chemistry and genetic implications of tourmaline and Li-F-Cs micas from the Valdeflores area (Caceres, Spain). Am. Mineral. 84 (1-2), 55–69.
Pollard, P.J., 2021. The Yichun Ta-Sn-Li Deposit, South China: Evidence for Extreme Chemical Fractionation in F-Li-P-Rich Magma. Econ. Geol. 116, 453–469.
Robert, J.-L., Beny, J.-M., Ventura, G.D., Hardy, M., 1993. Fluorine in micas: crystal-chemical control of the OH-F distribution between trioctahedral and dioctahedral sites. Eur. J. Mineral. 5 (1), 7–18.
Roda-Robles, E., Pesquera, A., Gil-Crespo, P., Torres-Ruiz, J., 2012. From granite to highly evolved pegmatite: A case study of the Pinilla de Fermoselle granite–pegmatite system (Zamora, Spain). Lithos 153, 192–207.
Rudnick, R.L., Gao, S., 2003. Composition of the continental crust. Treatise Geochem. 3, 1–64.
Seal, R.R., 2006. Sulfur isotope geochemistry of sulfide minerals. Rev. Mineral. Geochem. 61 (1), 633–677.
Simons, B., Andersen, J.C.Ø., Shail, R.K., Jenner, F.E., 2017. Fractionation of Li, Be, Ga, Nb, Ta, In, Sn, Sb, W and Bi in the peraluminous Early Permian Variscan granites of the Cornubian batholith: Precursor processes to magmatic-hydrothermal mineralization. Lithos 278, 491–512.
Stepanov, A., Hermann, J., 2013. Fractionation of Nb and Ta by biotite and phengite: Implications for the "missing Nb paradox". Geology 41, 303–306.
Stepanov, A., Mavrogenes, J.A., Meffre, S., Davidson, P., 2014. The key role of mica during igneous concentration of tantalum. Contrib. Miner. Petrol. 167, 2–8.
Sun, S.S., McDonough, W.F., 1989. Chemical and isotopic systematics of oceanic basalts: implication for mantle composition and processes. Geol. Soc. Lond. Spec. Pub. 42, 313–345.
Timofeev, A., Migdisov, A.A., Williams-Jones, A.E., 2015. An experimental study of the solubility and speciation of niobium in fluoride-bearing aqueous solutions at elevated temperature. Geochim. Cosmochim. Acta 158, 103–111.
Timofeev, A., Migdisov, A.A., Williams-Jones, A.E., 2017. An experimental study of the solubility and speciation of tantalum in fluoride-bearing aqueous solutions at elevated temperature. Geochim. Cosmochim. Acta 197, 294–304.
Tischendorf, G., Gottesmann, B., Förster, H.-J., Trumbull, R.B., 1997. On Li-bearing micas: estimating Li from electron microprobe analyses and an improved diagram for graphical representation. Mineral. Mag. 61 (409), 809–834.
Van Lichtervelde, M., Salvi, S., Beziat, D., Linnen, R.L., 2007. Textural features and fhemical evolution in tantalum oxides: magmatic versus hydrothermal origins for Ta mineralization in the Tanco Lower Pegmatite, Manitoba, Canada. Econ. Geol. 102, 257–276.
Van Lichtervelde, M., Grégoire, M., Linnen, R.L., Béziat, D., Salvi, S., 2008. Trace element geochemistry by laser ablation ICP-MS of micas associated with Ta mineralization in the Tanco pegmatite, Manitoba, Canada. Contrib. Mineral. Petrol. 155 (6), 791–806.
Wang, Y., Fan, W., Zhang, G., Zhang, Y., 2013. Phanerozoic tectonics of the South China Block: key observations and controversies. Gondwana Res. 23 (4), 1273–1305.
Wang, D., Huang, F., Wang, Y., He, H., Li, X., Liu, X., Sheng, J., Liang, T., 2020. Regional metallogeny of Tungsten-tin-polymetallic deposits in Nanling region, South China. Ore Geol. Rev. 120, 103305.
Wei, B.o., Wang, C.Y., Zhao, Z., Bao, H., 2020. Columbite-group minerals and mica of peraluminous granite record the magmatic-hydrothermal processes that formed the Zhaojinggou Ta-Nb deposit in the North China Craton. Lithos 370-371, 105648.
Wood, S.A., Samson, I.M., 2000. The hydrothermal geochemistry of tungsten in granitoid environments: I. Relative solubilities of ferberite and scheelite as a function of T, P, pH, and mNaCl. Econ. Geol. 95 (1), 143–182.
Wu, M., Samson, I.M., Zhang, D., 2017. Textural and chemical constraints on the formation of disseminated granite-hosted W-Ta-Nb mineralization at the Dajishan Deposit, Nanling Range, Southeastern China. Econ. Geol. 112 (4), 855–887.
Wu, M.Q., Samson, I.M., Zhang, D.H., 2018. Textural features and chemical evolution in Ta-Nb Oxides: implications for Deuteric Rare-Metal Mineralization in the Yichun Granite-Marginal Pegmatite, Southeastern China. Econ. Geol. 113, 937–960.
Xie, L., Wang, Z., Wang, R., Zhu, J., Che, X., Gao, J., Zhao, X.u., 2018. Mineralogical constraints on the genesis of W-Nb–Ta mineralization in the Laiziling granite (Xianghualing district, south China). Ore Geol. Rev. 95, 695–712.
Yin, R., Han, L., Huang, X.L., Li, J., Li, W.X., Chen, L.L., 2019. Textural and chemical variations of micas as indicators for tungsten mineralization: Evidence from highly evolved granites in the Dahutang tungsten deposit, South China. Am. Mineral. 104, 949–965.
Yuan, S.D., Williams-Jones, A.E., Romer, R.L., Zhao, P.L., Mao, J.W., 2019. Protolith-related thermal controls on the decoupling of Sn and W in Sn-W metallogenic provinces: insights from the Nanling region, China. Econ. Geol. 114, 1005–1012.
Zajacz, Z., Halter, W.E., Pettke, T., Guillong, M., 2008. Determination of fluid/melt partition coefficients by LA-ICPMS analysis of co-existing fluid and silicate melt inclusions: controls on element partitioning. Geochim. Cosmochim. Acta 72 (8), 2169–2197.
Zhao, G.C., Cawood, P.A., 2012. Precambrian geology of China. Precambr. Res. 222–223, 13–54.
Zhou, X., Sun, T., Shen, W., Shu, L., Niu, Y., 2006. Petrogenesis of Mesozoic granitoids and volcanic rocks in South China: a response to tectonic evolution. Episodes 29 (1), 26–33.
Zhu, J.-C., Li, R.-K., Li, F.-C., Xiong, X.-L., Zhou, F.-Y., Huang, X.-L., 2001. Topaz–albite granites and rare-metal mineralization in the Limu District, Guangxi Province, southeast China. Miner. Deposita 36 (5), 393–405.